Moisture transformation in Arctic warm airmass intrusions: process attribution with stable water isotopes

C.F. Brunello [1], F. Gebhardt [1,2], A. Rinke [1], M. Dütsch [3], S. Bucci [3], H. Meyer [1], M. Mellat [1], M. Werner [1]

[1] Alfred Wegener Institute, Helmholtz Centre for Polar and Marine Research, Germany
[2] Institute of Physics and Astronomy, Institute of Environmental Science and Geography, University of Potsdam, Germany
[3] Department of Meteorology and Geophysics, University of Vienna, Vienna, Austria

Abstract

Warm airmass intrusions (WAIs) from the mid-latitudes significantly impact the Arctic water budget. Here, we combine water vapor isotopes measurements from the MOSAiC expedition, with a Lagrangian-based process attribution diagnostic to track moisture origin and transformation in the central Arctic Ocean during two WAIs, under contrasting sea-ice concentrations (SIC). During winter with high SIC, two moisture states emerge: the local in-Arctic moisture, for which the isotope signal is influenced by kinetic processes in ice-cloud formation, is rapidly overprinted by low-latitude moisture advected poleward during WAI. In summer under low SIC, moisture is supplied through evaporation from land and ocean, with moisture distillation via liquid-cloud formation. The isotopic composition reflects the influence of higher humidity at the evaporation sites. Given the projected increase of frequency and duration of WAIs, our study contributes to assess process changes in the Arctic water cycle.

Plain Language Abstract

Intrusions of warm and moist airmasses from lower latitudes have a big effect on the Arctic climate system. We looked at data from the drifting MOSAiC expedition, where we measured the isotopic composition of water vapor. Water isotopes are powerful tracers of where moisture came from and how it changed during the transport. We focused on two specific warm air intrusions, occurring in February and September 2020 respectively, when the amount of sea ice was different. During the winter, we identified two sources of water: some moisture was influenced by in-Arctic processes and moisture exchanges with ice crystals in clouds, and some came from warmer places at lower latitudes. In the summer, when there was less sea ice, we found that water came mainly from evaporation over land and ocean. Our results show that the isotopic composition of vapor was influenced by how humid the places it came from were. As warm air intrusions are expected to happen more often and last longer in the future, our study helps us understand how they affect the Arctic water cycle.

Key points

- Airmass transformation during warm air intrusions depends on sea-ice extent
- During winter, warm air intrusions suppress moisture exchanges at the atmosphere-sea ice interphase
- In summer, d-excess is driven by vapor pressure gradients between ocean skin layer and the lower atmosphere at the evaporative sites

Keywords

Warm air intrusions, moisture transformation, stable water isotopes, Arctic water cycle, backward trajectories, sea ice

1. Introduction

Warm airmass intrusions (WAIs) are important drivers of heat and moisture transport into the Arctic (You et al., 2022; Papritz et al., 2022) and storm tracks are estimated to account for nearly three quarters of the average annual moisture transport (Fearon et al., 2021). The direct thermodynamic impacts of WAIs are increased downward fluxes of longwave radiation and sensible heat at the snow/ice surface, accompanied by a reduction in sea-ice concentration. The increased water vapor content resulting from warmer temperatures and higher frequency of moisture-carrying weather systems contributes to enhanced atmospheric heating. These transformations, among others, collectively drive what is known as Arctic Amplification, causing the Arctic to warm nearly four times the global average rate, with profound effects on local ecosystems and communities (IPCC, 2023). Thus, it is important to understand the consequences of WAIs on the Arctic water cycle.

The characteristics of each individual WAI depend on season, sourcing of the airmasses, characteristics of the atmospheric boundary layer (ABL) and surface conditions during the long-range transport. Importantly, WAIs can influence the Arctic sea ice (Li et al., 2022; Zhang et al., 2023) due to dynamic and thermodynamic processes, similar as cyclones and anticyclones do (Wernli and Papritz, 2018; Aue et al., 2022). However, to our knowledge no previous studies focused explicitly on how different conditions of sea ice affect the airmass moisture transformations during poleward transport from mid latitude into the Arctic.

During the poleward migration of airmasses over sea ice, radiative cooling is a key factor driving their transformation. Rapid cooling leads to turbulent mixing and the development of mixed-phase clouds. Eventually, the liquid water in the cloud precipitates, leaving behind a radiatively transparent ice-cloud (Ali and Pithan, 2020). Although WAIs are overall an important sink of atmospheric moisture, the redistribution of air by the atmospheric circulation is also a driver of intense evaporation from the ocean surface via the advection of cold air over relatively warmer ocean and strong near-surface winds (Papritz et al., 2015). These complex feedbacks, in combination with the limited observational data, challenge our understanding of these moisture exchange processes.

Stable water isotopes (SWI) serve as highly sensitive and integrated tracers of hydroclimatic changes, preserving information on the origin, transport, and transformation of water masses in the climate system. The strength of isotopic fractionation is inversely related to the temperature during water phase change processes, while differences in the diffusion rates of D and ^{18}O, described by the second order parameter deuterium excess, offer additional insights into changes in moisture sources (Dansgaard, 1964).

In light of the importance of WAIs and the potential insights offered by SWI, this study builds upon measurements performed during the Multidisciplinary drifting Observatory for the Study of Arctic Climate (MOSAiC) expedition (Shupe et al., 2022), during which the research vessel Polarstern (POL) was drifting in Arctic sea ice for one year. The study aims at identifying the physical drivers of the SWI changes observed during two WAI cases under contrasting seasonal conditions, during February and September 2020, and discusses how SWI can inform on the integrated moisture changes of the airmasses. The investigation is conducted by combining measured SWI, with a Lagrangian-based moisture diagnostic and process attribution method.

2. Methods

The measurements of this study refer to February and September 2020. During both these periods, POL was situated near the North Pole (Shupe et al., 2022), offering a chance to constrain spatial signal variability and assess the impact of different ambient conditions on water vapor transport.

2.1 Meteorological data

The local meteorological MOSAiC data used in this study were collected with related sensors located at different heights on board POL: relative humidity (RH) and air temperature (T) were measured at 29 m above sea level; air pressure (p) was measured at 19 m, but expressed at sea level. Specific humidity (q) is calculated based on RH, T and p. Continuous in-situ measurements of SWI were obtained from a Picarro L2140-i CRDS (Brunello et al., 2023). The calibrated and validated datasets are available at a 1-min averaged temporal resolution on PANGAEA (Schmithuesen, 2021a-d; Brunello et al., 2022a-d). Isotope concentrations are expressed in the usual δ-notation and deuterium excess is defined as d-excess = δD – 8 δ^{18}O.

We use meteorological variables from the European Centre for Medium-range Weather Forecasts (ECMWF) fifth-generation reanalysis (ERA5) reanalysis dataset (Hersbach et al., 2020) to characterize the environmental conditions during airmass transport. These parameters include 2 m air temperature (T_{2m}), mixing ratio, RH, SIC, land-sea mask, sea-surface temperature (SST), surface evaporation, and ABL height. All variables were extracted at 3 h temporal and 0.25 ° spatial resolutions, in the domain north of 40 °N latitude. For detailed analysis of sea-ice influence, the sea-ice concentration and lead ice fraction product AWI AMSR2 is used (Röhrs and Kaleschke, 2012).

2.2 Backward trajectories and process attribution

To represent the history of air parcels, meteorological parameters are traced along FLEXPART backward trajectories (Stohl et al., 2005; Pisso et al., 2019), based on ERA5. In this Lagrangian-based method, the release box is divided into finite elements of volume with equal mass which are called particles and are followed backward for an integration time of 30 days. The simulation was set up to release 100,000 particles every 3 h, equally distributed from a 0.1° × 0.1° × 100 m box moving with POL during the drift. FLEXPART is forced by horizontal and vertical wind components, temperature and specific humidity fields. In addition to the position and altitude of the particles, temperature and moisture were extracted for all individual trajectories up to 5 days backward in time. The moisture source diagnostic WaterSip (Sodemann et al., 2008; Fremme and Sodemann, 2019) is applied on the FLEXPART trajectories to estimate surface moisture uptakes weighted based on their contribution to humidity values at the target location. Results are aggregated on 0.5° x 0.5° gridded maps of dominant source regions at each time step.

As an air parcel is advected into the Arctic, it transforms from a warm and moist into a dry and cold airmass. Additional moisture can be taken up from land and ocean surfaces and moisture losses occur through adiabatic cooling, cloud formation and precipitation. Different airmasses with different history and origin can converge and mix. The isotopic composition of the parcel's water vapor is a passive tracer of all these exchanges, thus the contributions of each process type are key to understand the isotopic signature of the air parcel. Dütsch et al. (2018) developed a Lagrangian process attribution approach which relates SWI variations to key moisture exchange processes. Moisture losses are attributed to cloud formation and based on the temperature of the air parcel, the resulting cloud is classified as liquid, ice- or mixed-phase. Moisture increases are attributed to evaporation processes either from land or ocean, depending on the location of the air parcel. Here, we adapted this method to Arctic conditions, including uptake of moisture over sea ice and accounting for the presence of open leads. A detailed explanation of the process attribution, including our adaptation can be found in the Supporting Information (Text S1, Figure S1).

As a small addition, a process attribution evaluation of a single nudged ECHAM6-wiso simulation with explicit isotope diagnostic (Werner et al., 2011; Cauquoin and Werner, 2021) is included in Supporting Information (Text S2, Figure S4).

3. Results

3.1 Meteorological characterization of the two warm air intrusions

3.1.1 Meteorological characterization of the winter case (WAI1)

In February 2020, an anomalously intense cyclonic activity, with strong shifts in temperature and humidity, was observed (Rinke et al., 2021). Between February 9 and 25, three cyclones hit POL, with the strongest one related to a WAI, hereafter referred to as WAI1 taking place on February 16-20 (Figure 1a). The synoptic pattern was characterized by a low-pressure system over the northern North Atlantic/Barents Sea. On February 19, the cyclone travelled through the central Barents Sea, crossed the ice edge near Novaya Zemlya, before reaching the central Arctic. Strong pressure gradients in front of the cyclone led to the establishment of a poleward flow, bringing warm airmasses of around 0 °C. This was associated with transport of moist air over the Kara Sea, with values above 8 kg m^{-2}. This transport pattern was persistent during the next day, while the cyclone moved further to the east. The total water vapor map exhibits a narrow band of high-water vapor, where POL was located. Maximum temperature and specific humidity occurred February 20 midday with -15 °C and 1.4 g kg^{-1}, respectively. On February 21, the cyclone travelled northwards, while the dipole structure weakened. The warm air sector moved further eastward to the Canadian Arctic Archipelago. POL was located in colder and drier downwind airmasses of the cyclone, while warm and moist airmasses were wrapping around the cyclone center. Temperatures and humidity at POL exhibited a sudden drop by 10 °C and 0.6 g kg^{-1}, before rising again (Figure 2b).

3.1.2 Meteorological characterization of the summer case (WAI2)

In September 2020, the Arctic sea ice cover was at its annual minimum and transiting into regrowth state (Nicolaus et al., 2022) when two strong cyclonic events occurred. The first cyclone on September 13 lasted 1.5 days (hereafter referred to as WAI2a). Similar to the winter case, the tropospheric circulation was characterized by an anti-cyclone over Siberia and a developing cyclone in the Atlantic sector (Figure 1b). In the morning of September 13, the cyclone cut off from a low-pressure system over Scandinavia and started moving northwards through the Barents Sea. As it moved, pressure gradients to its front led to the advection of warm airmasses from Siberia and increase of the total column water vapor. In the afternoon it crossed the sea-ice edge and reached POL in the evening. Local temperature (Figure 2e) shifted from -9 to 0 °C and 3.7 g kg^{-1} humidity peaks were observed during the moist and warm spell. In the morning of September 14, the cyclone passed the ship, causing a sudden drop in temperature and humidity. While pressure gradients weakened, 850 hPa-temperature fields indicated warm air parcels (ca. 0 °C) wrapped around the cyclone center. This led to persistent warmer and moist air conditions during the following two days. A second cyclone with similar track occurred during September 23-25 (WAI2b) and caused a strong local temperature increase of about 14 °C.

3.2 Backward trajectory analyses

3.2.1 Transport conditions during the winter case (WAI1)

To illustrate the typical ambient conditions during the transport of the airmasses, Figure 1c illustrates temperature, humidity and surface conditions along the center-of-mass trajectory, as calculated by FLEXPART2 based on ERA5, during the first peak of WAI1. Note that surface moisture uptakes are based on aggregated maps (Section 2.2). Due to the lack of backward time information, values may not correspond to the real uptakes of the air parcels and should be interpreted with caution. Four days before arrival (-84 h), the vertical temperature column indicates a 2 km thick layer of warm (0-5 °C) air. This layer is characterized by low-level mixed-phase clouds with a dominance of liquid-water content. The crossing of the ice edge in the coastal area at around -60 h did not lead to an up-gliding of the airmasses and the presence of low-level mixed-phased clouds was sustained. Liquid water droplets are largely opaque in longwave radiation, shifting major cooling to the cloud top, causing the formation of a temperature inversion at around 1.5 km altitude. At around -36 h, WaterSip reveals a moisture uptake reflected in a small increase in the averaged specific humidity of the air parcels. This uptake does not appear to be linked to changes in the underlying sea-ice conditions or topography. Our analysis indicates that the center-of-mass trajectory reached the northern end of Novaya Zemlya at this time, where the open sea extended deep into the Arctic sea-ice region (Figure 1a). Hence, moisture increases could be attributed to mixing with moist airmasses associated with the sea-ice marginal area. This mixing is accompanied by a sudden drop in altitude of the air parcels and an elevation change of the lower cloud layers, which could be due to stronger turbulent mixing. During the last 24 hours before arrival at POL, the low-level clouds begin to dissipate and moisture uptakes are small. The temperature and cloud water columns suggest a moderate up-gliding of the lower airmasses during the last 12 hours, reestablishing a near-surface temperature inversion.

3.2.2 Transport conditions during the summer case (WAI2)

Figure 1d illustrates the conditions along the center-of-mass trajectory during the first peak of WAI2. The early phase of the cyclone passage was marked by a strong poleward flow originating from western Siberia. During the advection over the continent, the airmass had a temperature exceeding 10 °C and travelled up to 3 km altitude. At ground level, temperatures were at ca. 20 °C and surface moisture uptakes were identified. During this period, there was only little cloud formation with mixed-phase clouds above 1 km altitude and high-level ice-clouds. 60 h before arrival, the airmasses reached the coastal area, leading to strong moisture uptakes over the relatively colder ocean. The average humidity of the air parcels increased to 6.4 g kg^{-1}. From 48 h to 24 h, the air parcels primarily traveled over open ocean without additional uptakes. A decrease in temperature in the lowest 100 m reflects the cooling of the airmasses over the ocean, while increases are linked to passing of land. Although the passing of land likely induced some vertical lifting, most air parcels stayed below 500 m altitude. At -12 h, the air parcels crossed the sea-ice edge. The temperature column indicates a lifting of warmer airmasses, suggesting upgliding over colder airmasses over the sea ice, in agreement with Komatsu et al. (2018). Near-surface temperatures showed values around 0 °C potentially linked to melting processes, while the advected warm air created an elevated temperature inversion aloft. Abundant liquid cloud formation dominates the lower level of the atmosphere. As previously observed by Kirbus et al. (2023), the formation of low-level liquid cloud was accompanied by a separated formation of high-level ice-clouds. Despite WaterSip identifying small uptakes over sea ice, the strong low-level cloud formation resulted in a net moisture decrease of ca. 2.5 g kg^{-1}.

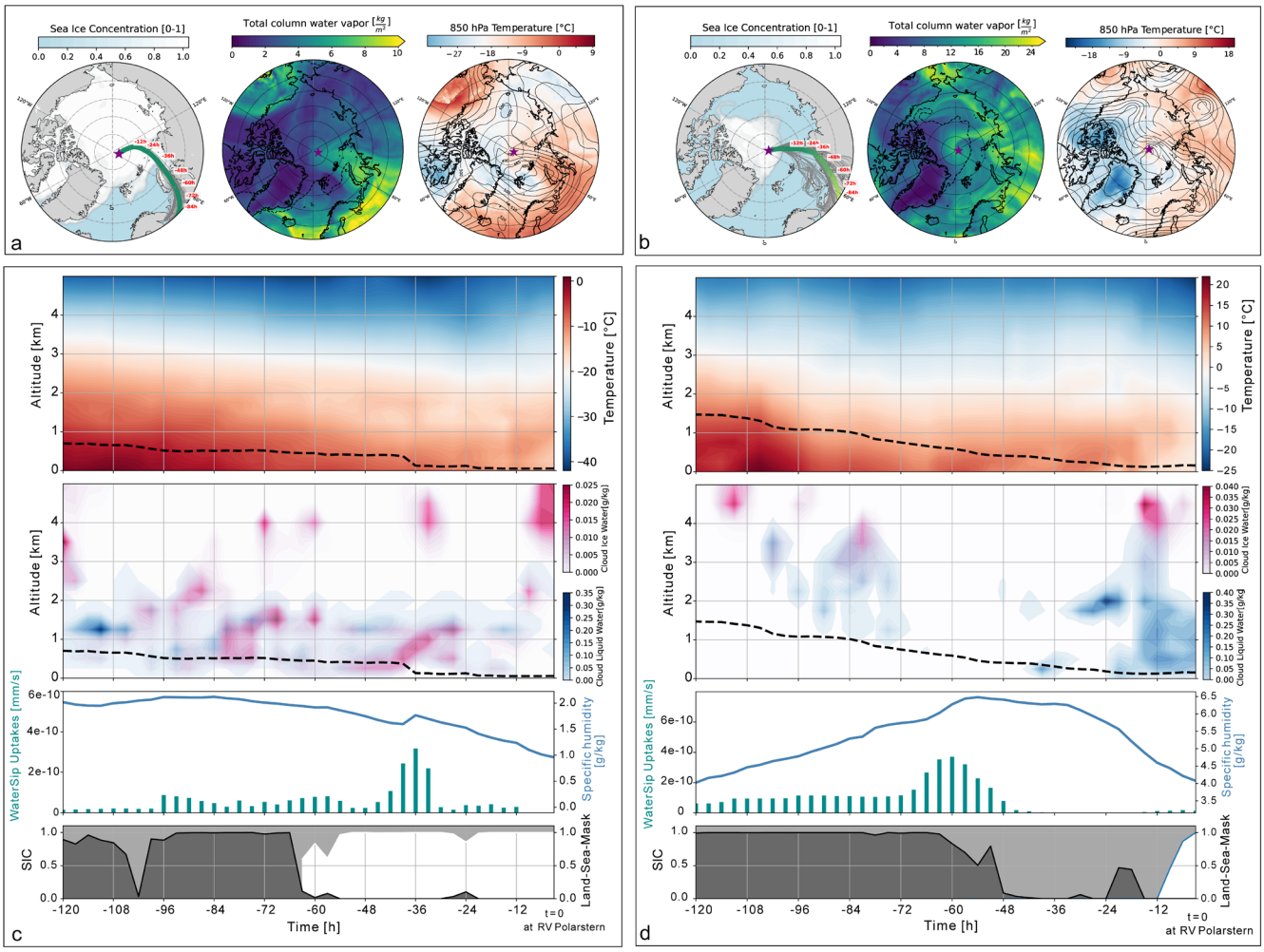

Figure 1. *Upper panels:* Synoptic *overview of WAI1(a) and WAI2a (b), including maps of sea-ice concentration with the individual trajectories (gray) and their center-of-mass (thick, green line) advected to POL, the total column water vapor and the combined maps of 500-hPa geopotential heights (contour lines) and 850-hPa temperatures (color shading), retrieved from ERA5. The maps were generated using data from February 19, 00 h (peak WAI1) and September 13, 21 h (peak WAI2a), respectively and the position of POL at those times is marked by a purple star.*

Lower panels: Conditions along the center-of-mass trajectory during peaks of WAI1 (c) and WAI2a (d), as retrieved from ERA5. Negative signs on the x-axis indicate hours before arrival at POL. The two upper panels show columns of temperature and cloud ice content (pink) and liquid water content (blue). The black dashed line indicates the height of the center-of-mass trajectory. The third panels from the top, show uptakes identified by WaterSip (turquoise bars) and the average humidity of the air parcels (blue line). The lowermost panels represent sea-ice concentration (white fill) and land-sea mask (dark grey fill).

3.3 Process attribution

The upper panels of Figure 2 illustrate the results of our process attribution approach (Section 2.2), based on ERA5 and AMSR2. Both uptakes and losses are shown as positive contributions to the total amount of moisture exchanges along the trajectories (Supporting Information, Text S1.2).

3.3.1 Moisture processes during the winter case (WAI1)

The process attribution during February 2020 reveals a substantial overall contribution of evaporation over sea ice, exceeding 40 % of the total exchange, with only minor contributions from lead-dominated sea ice (1-

5 %). There is consistent moisture gain, accounting for ~20-30 % of changes, through 'mixing-in', referring to moisture uptake in the free troposphere. This contribution shows slightly higher values during cold, non-WAI, phases. Peak values of contribution of land evaporation are found during a smaller intrusion on February 14, and during WAI1, reaching values of about 20 %. Moisture losses are dominated by ice-cloud formation, accounting for about 30 %. The contribution of mixed-phase clouds during the non-WAI phases is small but variable (5-20 %). During WAI1, losses due to ice-clouds dissolution and mixed-phase cloud formation becomes the dominant moisture loss process. After the intrusion, uptakes suddenly shift to evaporation over sea ice, while humidity decreases abruptly. Shortly after, the peak in ocean evaporation can be linked to the inflow of airmasses from the backside of the cyclone. During the following days, moisture exchanges are dominated by ocean uptakes and mixed-phase cloud formation, with only little ice-cloud formation and small contributions of sea-ice evaporation. This suggests, that the impact of WAI1 was able to sustain a cloudy moist state at POL until the end of the period.

Q*ex*p (Figure 2b) quantifies the amount of moisture attributed to a process, and only refers to moisture tracked within the last 5 days of transport. *Qex*p was close to observed q before and after WAI1, indicating enhanced uptakes in the last part of the transport. However, in the beginning of the intrusion on February 18, *qexp* is low, indicating that the initial moisture content of the air parcel was already high and uptakes in the last 5 days of transport did not contribute significantly to the absolute total moisture content.

3.3.2 Moisture processes during the summer case (WAI2)

During WAI2, moisture is predominantly supplied by evaporation from the ocean, accounting for 20-60 % of the humidity changes (Figure 2d). Contributions from sea-ice dominated regions are high during short periods but drop to zero when contribution from ocean evaporation occurs. This behavior may be related to changes in wind directions, given that sea ice persists mainly in the western Arctic (Greenland, Canadian Archipelago), while the Kara and Barents Sea are ice-free. When uptake from sea ice takes place, there is a low, but stable contribution of evaporation from leads (5 %). Continental moisture sources are primarily identified during the two WAIs. Contributions from mixing processes display higher variability compared to the winter case. From September 11-13, mixing plays a minor role, but as WAI2a begins, it exhibits a persistent contribution of 10-30 % until WAI2b when ocean evaporation accounts for the majority of the uptakes. Moisture losses are primarily driven by mixed-phase cloud formation, dominating during non-WAI phases, and liquid cloud formation during the WAIs.

Qexp (Figure 2e) is always lower than the observed humidity, indicating a strong contribution of moisture uptakes prior to the last 5 days of transport and the long-distance advection of the summer moisture, independently of the WAIs.

3.4 Isotopic characterization of the two warm air intrusions

3.4.1 Isotopic characterization of the winter case (WAI1)

During WAI1 (Figure 2c), we observed strong variations in $\delta^{18}O$ of vapor at POL. During cold phases, the air was more depleted with $\delta^{18}O$ around -40 ‰. Injections of warm moist air, as during February 14-16, and the strong intrusion on February 18-21, led to increases of $\delta^{18}O$ by about 5-10 ‰. During the WAI $\delta^{18}O$ reached its maximum of -32 ‰ after the peak in temperature and humidity. The time lag may indicate additional processes rather than only a temperature effect. $\delta^{18}O$ remained stable at -34 ‰ during the following 2 days, before a sudden decrease to around -40 ‰. For d-excess, we observed an overall positive correlation (r = 0.51) with $\delta^{18}O$. However, d-excess seems to be more sensitive to little injections of warmer air. Two small temperature increases during February 14 and 16 led to strong d-excess increases by about 15 ‰. During

the main WAI1 on February 18-21, d-excess increased up to 5 ‰ and stabilized around that value already 12 h before the humidity peak. Both d-excess and $\delta^{18}O$ exhibit two different modes with high values during moist injections and low values in cold and dry phases.

3.4.2 Isotopic characterization of the summer case (WAI2)

During September 2020, the WAIs brought isotopically-enriched moisture to POL, causing $\delta^{18}O$ in vapor to increase by more than 20 ‰ while the relatively cold-phases before and after were characterized by isotopically-depleted moisture (-30 ‰) (Figure 2f). Hence, isotope changes largely follow the temperature and moisture evolution linked to this synoptic event. During cold-phases (Sep 11-13 and Sep 15-20), $\delta^{18}O$ minima are reached in coincidence with temperature and humidity, while during both WAIs (Sep 11-13 and Sep 15-20), the peak in $\delta^{18}O$ had a time-lag of 12-24 h. D-excess ranges between -13 ‰ and +15 ‰ and it is strongly anti-correlated (r = -0.93) to $\delta^{18}O$, especially during the WAIs.

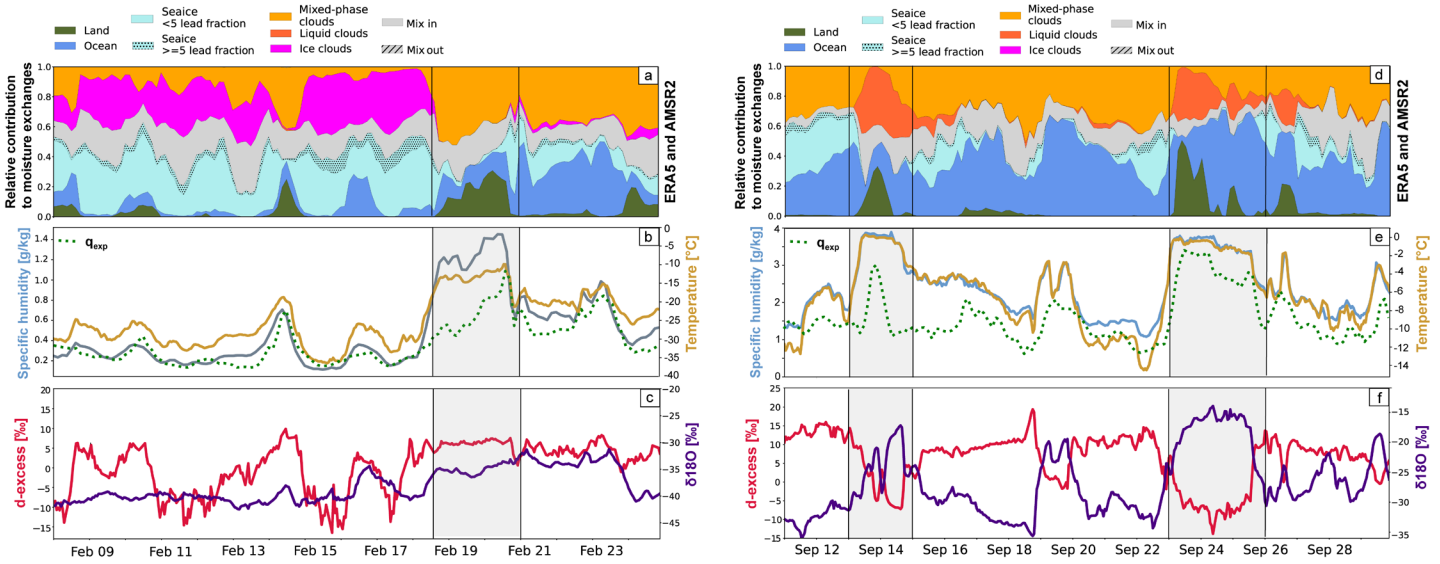

Figure 2. *Results of the process attribution diagnostic for the winter case (left) and summer case (right) based on ERA5 and AMSR-2. WAI1, WAI2a and WAI2b are highlighted by vertical black lines. In the middle panels, observed humidity (light blue) and temperature (yellow) measured at POL are shown. The green dotted line in panel indicates q_{exp}, i.e. the amount of moisture which was taken up along the 5-day trajectories, and assigned to the given processes. The lowest panels present observed local d-excess and $\delta^{18}O$ as measured onboard POL.*

4. Discussion and Conclusions

4.1 WAIs overprint low background d-excess in winter

During February 2020, d-excess shifted between two modes. One mode exhibits d-excess values around 5 ‰, and corresponds to injections of warm moist air sourced from ocean and land evaporation from lower latitudes and accompanied by formation of mixed-phase clouds. This contrasts with a second mode, characterized by very low $\delta^{18}O$ values around -10 to -15 ‰ during the coldest and driest phases not influenced by WAIs. These phases are characterized by a dominance in uptakes over sea ice and 'mixing in', while moisture decreases are mostly due to ice-cloud formation. This results into positive correlation between d-excess and $\delta^{18}O$ which is in striking contrast to the opposite relationship observed during the summer WAI (Figure 2f).

Kopec et al. (2019) and Leroy–Dos Santos et al. (2020) observed similar positive relation during winter at the Greenland's coast line and on Svalbard. Kopec et al. (2019) argue that low d-excess in Greenland precipitation is a result of a non-linear Rayleigh distillation with progressive decreasing d-excess in the earlier stage, in combination with kinetic effects during supersaturation in ice- and mixed-phase clouds. This is in agreement with our process attribution analysis, where we find a negative correlation of d-excess with ice-cloud formation (r = -0.72). Ice droplets in clouds grow by vapor deposition under supersaturated conditions involving kinetic fractionation (Samuels-Crow et al., 2014; Galewsky, 2015). The effect is expected to strongly decrease d-excess values in the remaining vapor phase. Furthermore, 5-day trajectory analyses for the days February 15-18, when low d-excess values were observed, show that airmasses resided the entire time, over sea ice. Such cold and stable conditions are typically associated with clear sky and strong temperature inversions (Jozef et al., 2023), which can lead to vapor deposition onto the ice. During polar summers, diurnal cycles between vapor deposition and sublimation result in lower d-excess amplitude during night-time stable ABL conditions (Casado et al., 2016; Ritter et al., 2016). Although this process may apply to the Arctic polar night, solid deposition cannot be discriminated by our process attribution algorithm, since there is no distinction between ice-cloud formation within the ABL and vapor deposition to the surface. A second process which correlates with moisture exchange during cold phases is evaporation from sea-ice dominated areas (r = -0.51 for high lead fraction). However, moisture originating over sea-ice dominated regions is typically imprinted with high d-excess values (Kurita et al., 2016; Bonne et al., 2019; Leroy–Dos Santos et al., 2020), ruling out the influence of lead evaporation on our low d-excess observations. In conclusion, we propose that primarily ice-cloud formation, in combination with vapor deposition and Rayleigh distillation, is causing the unusual negative d-excess values in near-surface water vapor in the winter Arctic.

Low d-excess values increase abruptly whenever moist and warm airmasses are advected. This can be explained by a shift towards mid-latitude moisture where d-excess values around 10-15 ‰ are typically measured (Galewsky et al., 2016; Bastrikov et al., 2014). Evaporation from the ocean surface under relatively cold conditions, with steeper surface temperature gradients as compared to Arctic winter conditions, yields higher d-excess values due to enhanced kinetic fractionation.

4.2 Source conditions dominate d-excess during summer

During summer, SWI changes at POL generally follow the evolution of local temperature and humidity (Brunello et al., 2023). Before and after the pulses of warm air by WAIs, low $\delta^{18}O$ values mimic relatively low temperature and humidity. During these times, significant negative correlation is found between $\delta^{18}O$ changes and mixed-phase cloud formation (r = -0.66). This suggests stronger degrees of distillation during cold-phase, causing depleted $\delta^{18}O$ in vapor. The low $\delta^{18}O$ values are usually accompanied by maxima in d-excess around 10-15 ‰. This observation aligns with Bonne et al. (2019) and Leroy–Dos Santos et al. (2020). Figure S2 (Supporting Information) illustrates the correlations of d-excess with contributions of moisture uptake from sea ice. The linear relation between d-excess and evaporation over sea ice with low lead fraction agrees with the relationship identified by Bonne et al. (2019). Contributions of evaporation over sea ice with higher lead fraction are generally too low for meaningful interpretation, but the determined steeper slope could be explained by the presence of open-water bodies where evaporation is associated with strong kinetic fractionation. High d-excess values are commonly formed at the sea-ice margin and along coastlines, where cold dry airmasses are advected over the relatively warm ocean. This results in a strong kinetic fractionation due to the vapor pressure differences between the saturated skin layer of the ocean and the air aloft (Steen-Larsen et al., 2014; Galewsky et al., 2016). Extracted source conditions at uptake locations partly support

this hypothesis (Figure S3, Supporting Information) as we find significant correlations (r = -0.49) between d-excess and relative humidity calculated with respect to sea-surface temperature (RH_{SST}).

The pre/post WAIs low $\delta^{18}O$/high d-excess values contrast with high $\delta^{18}O$/low d-excess observed during the WAIs. These events are marked by large contributions of land evaporation. However, minima in d-excess are reached before and after the peak contribution of land evaporation when ocean uptakes contribute to an increasing humidity level. D-excess values settle back to values around 0 ‰ when land evaporation overprints ocean evaporation. The center-of-mass trajectory (Fig. 2b) shows the respective timestep of the first minimum, revealing that major uptakes happened in the coastal region, where the warm airmasses (>15 °C) experience a reduction of kinetic effects and low d-excess. In contrast, the correlation of d-excess to contributions of ocean evaporation is not significant. This is presumably due to the fact that the process attribution does not differentiate between the various environmental conditions under which uptakes over the ocean can happen.

To further investigate the impact of evaporation on the final d-excess composition of the airmasses, we extracted the most relevant surface environmental parameters at the moisture source regions. We found that d-excess correlates negatively with T_{2m} (r = -0.65), and positively to SST (r = 0.47). The correlation to RH is not significant indicating that RH alone cannot explain kinetic processes during uptakes from the ocean. However, both RH_{SST} and T_{2m}−SST show negative correlation to d-excess in agreement with the finding of Pfahl and Wernli (2008) in the Mediterranean basin. However, the correlation coefficient to RH_{SST} (r = -0.49) and the slope of the linear relationship (-0.31 ‰/%) are lower compared to their findings (r = -0.82 and -0.53 ‰/%, respectively). The observed slope of -0.39 ‰/% for the whole Atlantic found by Bonne et al. (2019), on the other hand, is closer to our results. The combination of strong negative relationship to T_{2m}, positive relation to SST, and the negative relation to T_{2m}−SST and RH_{SST} respectively, confirms that the d-excess variability in summer is mostly driven by vapor pressure gradients between the ocean skin layer and the lower atmosphere. We conclude that kinetic effects during the vapor transport were not sufficient to overprint the individual d-excess fingerprint of the oceanic moisture, and that the source signal of d-excess is largely conserved during the transport into the Arctic.

4.3 Modelling of Arctic cloud processes in ECHAM6-wiso

A nudged ECHAM6-wiso simulation revealed biases when compared to measured $\delta^{18}O$ and d-excess during MOSAiC (Brunello et al., 2023). To distinguish whether the SWI are not well simulated due to missing or mis-represented fractionation processes, or due to biased atmospheric conditions, we repeated the process attribution analysis using modelled ECHAM6-wiso fields, instead of ERA5 (Text S2, Supporting Information). This supplementary analysis suggests a deficit in ECHAM6-wiso to capture cloud formation of ice- and mixed-phase clouds along the trajectories with the largest deficits during winter cold conditions. Cloud processes in the Arctic are complex and key controls are cloud microphysics, availability of condensation nuclei and cloud-surface-interactions, which are challenges in global models (Sotiropoulou et al., 2016). Furthermore, in ECHAM6-wiso, the SWI fractionation during ice-crystal formation under supersaturated conditions is parameterized by adjusting the equilibrium fractionation factor of $\delta^{18}O$ and δD, following Jouzel and Merlivat (1984). The latter is solely dependent on temperature during water phase change, which might be an oversimplification of this process (Dütsch et al., 2019).

We conclude that that an improved representation of ABL dynamics and refining the environmental conditions during water vapor uptake and deposition could contribute to more accurate simulations of moisture transformation. The presented initial short evaluation study shown is intended to motivate further throughout model investigation.

Open research

The MOSAiC isotope datasets are available on PANGAEA at: doi.org/10.1594/PANGAEA.951424, doi.org/10.1594/PANGAEA.951446, doi.org/10.1594/PANGAEA.951447, doi.org/10.1594/PANGAEA.951448, doi.org/10.1594/PANGAEA.951449

Trajectory analysis from the FLEXPART model simulations were performed at the University of Vienna and can be accessed at: https://img.univie.ac.at/webdata/mosaic.

ECMWF reanalysis data can be downloaded freely from the Copernicus Climate Change Service, Climate Data Store: https://cds.climate.copernicus.eu/cdsapp#!/dataset/reanalysis-era5-single-levels?tab=form

The ECHAM6-wiso simulation was performed at the Alfred Wegener Institute. The ECHAM model code is available under a version of the MPI-M software license agreement.

Acknowledgments

CFB, MW, MM, and HM acknowledge support from BMBF grant 03F0869A (CiASOM). AR acknowledges funding by BMBF grant 03F0872A (SynopSys), DFG grant 268020496 (AC3) and EU H2020 grant 101003590 (PolarRES). The data used in this manuscript were produced as part of MOSAiC20192020. We thank all those who contributed to MOSAiC (Nixdorf et al. 2021).

References

Ali, S. M., & Pithan, F. (2020). Following moist intrusions into the Arctic using SHEBA observations in a Lagrangian perspective. Quarterly Journal of the Royal Meteorological Society, 146(732), 3522-3533.

Aue, L., Vihma, T., Uotila, P., & Rinke, A. (2022). New insights into cyclone impacts on sea ice in the Atlantic sector of the Arctic Ocean in winter. Geophysical Research Letters, 49(22), e2022GL100051.

Bastrikov, V., Steen-Larsen, H., Masson-Delmotte, V., Gribanov, K., Cattani, O., Jouzel, J., & Zakharov, V. (2014). Continuous measurements of atmospheric water vapour isotopes in western Siberia (Kourovka). Atmospheric Measurement Techniques, 7(6), 1763-1776.

Bonne, J.-L., Behrens, M., Meyer, H., Kipfstuhl, S., Rabe, B., Schönicke, L., . . . Werner, M. (2019). Resolving the controls of water vapour isotopes in the Atlantic sector. Nature Communications, 10(1), 1632.

Brunello, C. F., Werner, M., Meyer, H., Mellat, M., & Bonne, J.-L. (2022a). Continuous near-surface atmospheric water vapour isotopic composition from Polarstern cruise PS122-1 (MOSAiC). PANGAEA. https://doi.org/10.1594/PANGAEA.951424

Brunello, C. F., Werner, M., Meyer, H., Mellat, M., & Bonne, J.-L. (2022b). Continuous near-surface atmospheric water vapour isotopic composition from Polarstern cruise PS122-2 (MOSAiC). PANGAEA. https://doi.org/10.1594/PANGAEA.951446

Brunello, C. F., Werner, M., Meyer, H., Mellat, M., & Bonne, J.-L. (2022c). Continuous near-surface atmospheric water vapour isotopic composition from Polarstern cruise PS122-3 (MOSAiC). PANGAEA. https://doi.org/10.1594/PANGAEA.951447

Brunello, C. F., Werner, M., Meyer, H., Mellat, M., & Bonne, J.-L. (2022d). Continuous near-surface atmospheric water vapour isotopic composition from Polarstern cruise PS122-4 (MOSAiC). PANGAEA. https://doi.org/10.1594/PANGAEA.951448

Brunello, C. F., Werner, M., Meyer, H., Mellat, M., & Bonne, J.-L. (2022e). Continuous near-surface atmospheric water vapour isotopic composition from Polarstern cruise PS122-5 (MOSAiC). PANGAEA. https://doi.org/10.1594/PANGAEA.951449

Brunello, C. F., Meyer, H., Mellat, M., Casado, M., Bucci, S., Dütsch, M., & Werner, M. (2023). Contrasting Seasonal Isotopic Signatures of Near-Surface Atmospheric Water Vapor in the Central Arctic During the MOSAiC Campaign. Journal of Geophysical Research: Atmospheres, 128(24), e2022JD038400.

Casado, M., Landais, A., Picard, G., Münch, T., Laepple, T., Stenni, B., . . . Genthon, C. (2016). Archival of the water stable isotope signal in East Antarctic ice cores. The Cryosphere Discussions, 2016, 1-33.

Casado, M., Landais, A., Picard, G., Münch, T., Laepple, T., Stenni, B., . . . Genthon, C. (2016). Archival of the water stable isotope signal in East Antarctic ice cores. The Cryosphere Discussions, 2016, 1-33.

Cauquoin, A., & Werner, M. (2021). High-Resolution Nudged Isotope Modeling With ECHAM6-Wiso: Impacts of Updated Model Physics and ERA5 Reanalysis Data. Journal of Advances in Modeling Earth Systems, 13(11), e2021MS002532.

Dansgaard, W. (1964). Stable isotopes in precipitation. Tellus, 16(4), 436-468.

Dütsch, M., Pfahl, S., Meyer, M., & Wernli, H. (2018). Lagrangian process attribution of isotopic variations in near-surface water vapour in a 30-year regional climate simulation over Europe. Atmospheric Chemistry and Physics, 18(3), 1653-1669.

Fearon, M. G., Doyle, J. D., Ryglicki, D. R., Finocchio, P. M., & Sprenger, M. (2021). The role of cyclones in moisture transport into the Arctic. Geophysical Research Letters, 48(4), e2020GL090353.

Galewsky, J. (2015). Constraining supersaturation and transport processes in a South American cold-air outbreak using stable isotopologues of water vapor. Journal of the Atmospheric Sciences, 72(5), 2055-2069.

Giorgetta, M. A., Roeckner, E., Mauritsen, T., Bader, J., Crueger, T., Esch, M., . . . Kinne, S. (2013). The atmospheric general circulation model ECHAM6-model description.

Graham, R. M., Hudson, S. R., & Maturilli, M. (2019). Improved performance of ERA5 in Arctic gateway relative to four global atmospheric reanalyses. Geophysical Research Letters, 46(11), 6138-6147.

Hersbach, H., Bell, B., Berrisford, P., Hirahara, S., Horányi, A., Muñoz-Sabater, J., . . . Schepers, D. (2020). The ERA5 global reanalysis. Quarterly Journal of the Royal Meteorological Society, 146(730), 1999-2049.

IPCC, 2023: Climate Change 2023: Synthesis Report. Contribution of Working Groups I, II and III to the Sixth Assessment Report of the Intergovernmental Panel on Climate Change [Core Writing Team, H. Lee and J. Romero (eds.)]. IPCC, Geneva, Switzerland, pp. 35-115, doi: 10.59327/IPCC/AR6-9789291691647.

Jouzel, J., & Merlivat, L. (1984). Deuterium and oxygen 18 in precipitation: Modeling of the isotopic effects during snow formation. Journal of Geophysical Research: Atmospheres, 89(D7), 11749-11757.

Jozef, G. C., Klingel, R., Cassano, J. J., Maronga, B., de Boer, G., Dahlke, S., & Cox, C. J. (2023). Derivation and compilation of lower atmospheric properties relating to temperature, wind, stability, moisture, and surface radiation budget over the central Arctic sea ice during MOSAiC. Earth System Science Data Discussions, 2023, 1-23.

Kirbus, B., Tiedeck, S., Camplani, A., Chylik, J., Crewell, S., Dahlke, S., . . . Handorf, D. (2023). Surface impacts and associated mechanisms of a moisture intrusion into the Arctic observed in mid-April 2020 during MOSAiC. Frontiers in Earth Science, 11, 1147848.

Kopec, B., Feng, X., Posmentier, E., & Sonder, L. (2019). Seasonal deuterium excess variations of precipitation at Summit, Greenland, and their climatological significance. Journal of Geophysical Research: Atmospheres, 124(1), 72-91.

Kretzschmar, J., Salzmann, M., Mülmenstädt, J., & Quaas, J. (2019). Arctic clouds in ECHAM6 and their sensitivity to cloud microphysics and surface fluxes. Atmospheric Chemistry and Physics, 19(16), 10571-10589.

Krumpen, T., Birrien, F., Kauker, F., Rackow, T., von Albedyll, L., Angelopoulos, M., . . . Dethloff, K. (2020). The MOSAiC ice floe: sediment-laden survivor from the Siberian shelf. The Cryosphere, 14(7), 2173-2187.

Kurita, N., Nakatsuka, T., Ohnishi, K., Mitsutani, T., & Kumagai, T. o. (2016). Analysis of the interdecadal variability of summer precipitation in central Japan using a reconstructed 106 year long oxygen isotope record from tree ring cellulose. Journal of Geophysical Research: Atmospheres, 121(20), 12,089-012,107.

Li, L., Cannon, F., Mazloff, M. R., Subramanian, A. C., Wilson, A. M., & Ralph, F. M. (2024). Impact of atmospheric rivers on Arctic sea ice variations. The Cryosphere, 18(1), 121-137.

Leroy-Dos Santos, C., Masson-Delmotte, V., Casado, M., Fourré, E., Steen-Larsen, H., Maturilli, M., . . . Minster, B. (2020). A 4.5 year-long record of Svalbard water vapor isotopic composition documents winter air mass origin. Journal of Geophysical Research: Atmospheres, 125(23), e2020JD032681.

Nicolaus, M., Perovich, D. K., Spreen, G., Granskog, M. A., von Albedyll, L., Angelopoulos, M., . . . Bessonov, V. (2022). Overview of the MOSAiC expedition: Snow and sea ice. Elem Sci Anth, 10(1), 000046.

Nixdorf, U., Dethloff, K., Rex, M., Shupe, M., Sommerfeld, A., Perovich, D. K., ... & Boetius, A. (2021). MOSAiC extended acknowledgement.

Papritz, L., Hauswirth, D., & Hartmuth, K. (2022). Moisture origin, transport pathways, and driving processes of intense wintertime moisture transport into the Arctic. Weather and Climate Dynamics, 3(1), 1-20.

Papritz, L., Pfahl, S., Sodemann, H., & Wernli, H. (2015). A climatology of cold air outbreaks and their impact on air–sea heat fluxes in the high-latitude South Pacific. Journal of Climate, 28(1), 342-364.

Pfahl, S., & Wernli, H. (2008). Air parcel trajectory analysis of stable isotopes in water vapor in the eastern Mediterranean. Journal of Geophysical Research: Atmospheres, 113(D20).

Pisso, I., Sollum, E., Grythe, H., Kristiansen, N. I., Cassiani, M., Eckhardt, S., . . . Groot Zwaaftink, C. D. (2019). The Lagrangian particle dispersion model FLEXPART version 10.4. Geoscientific Model Development, 12(12), 4955-4997.

Rinke, A., Cassano, J. J., Cassano, E. N., Jaiser, R., & Handorf, D. (2021). Meteorological conditions during the MOSAiC expedition: Normal or anomalous? Elem Sci Anth, 9(1), 00023.

Ritter, F., Steen-Larsen, H. C., Werner, M., Masson-Delmotte, V., Orsi, A., Behrens, M., . . . Kipfstuhl, S. (2016). Isotopic exchange on the diurnal scale between near-surface snow and lower atmospheric water vapor at Kohnen station, East Antarctica. The Cryosphere, 10(4), 1647-1663.

Samuels-Crow, K. E., Galewsky, J., Hardy, D. R., Sharp, Z. D., Worden, J., & Braun, C. (2014). Upwind convective influences on the isotopic composition of atmospheric water vapor over the tropical Andes. Journal of Geophysical Research: Atmospheres, 119(12), 7051-7063.

Schmithüsen, H. (2021a). Continuous meteorological surface measurement during POLARSTERN cruise PS122/1. Alfred Wegener Institute, Helmholtz Centre for Polar and Marine Research. https://doi.org/10.1594/PANGAEA.935221

Schmithüsen, H. (2021b). Continuous meteorological surface measurement during POLARSTERN cruise PS122/2. Alfred Wegener Institute, Helmholtz Centre for Polar and Marine Research. https://doi.org/10.1594/PANGAEA.935222

Schmithüsen, H. (2021c). Continuous meteorological surface measurement during POLARSTERN cruise PS122/3. Alfred Wegener Institute, Helmholtz Centre for Polar and Marine Research. https://doi.org/10.1594/PANGAEA.935223

Schmithüsen, H. (2021d). Continuous meteorological surface measurement during POLARSTERN cruise PS122/4. Alfred Wegener Institute, Helmholtz Centre for Polar and Marine Research. https://doi.org/10.1594/PANGAEA.935224

Schmithüsen, H. (2021e). Continuous meteorological surface measurement during POLARSTERN cruise PS122/5. Alfred Wegener Institute, Helmholtz Centre for Polar and Marine Research. https://doi.org/10.1594/PANGAEA.935225

Shupe, M. D., Rex, M., Blomquist, B., Persson, P. O. G., Schmale, J., Uttal, T., . . . Bariteau, L. (2022). Overview of the MOSAiC expedition: Atmosphere. Elem Sci Anth, 10(1), 00060.

Sotiropoulou, G., Sedlar, J., Forbes, R., & Tjernström, M. (2016). Summer Arctic clouds in the ECMWF forecast model: An evaluation of cloud parametrization schemes. Quarterly Journal of the Royal Meteorological Society, 142(694), 387-400.

Stohl, A., Forster, C., Frank, A., Seibert, P., & Wotawa, G. (2005). The Lagrangian particle dispersion model FLEXPART version 6.2. Atmospheric Chemistry and Physics, 5(9), 2461-2474.

Werner, M., Langebroek, P. M., Carlsen, T., Herold, M., & Lohmann, G. (2011). Stable water isotopes in the ECHAM5 general circulation model: Toward high-resolution isotope modeling on a global scale. Journal of Geophysical Research: Atmospheres, 116(D15).

Wernli, H., & Papritz, L. (2018). Role of polar anticyclones and mid-latitude cyclones for Arctic summertime sea-ice melting. Nature Geoscience, 11(2), 108-113.

You, C., Tjernström, M., & Devasthale, A. (2022). Warm and moist air intrusions into the winter Arctic: a Lagrangian view on the near-surface energy budgets. Atmospheric Chemistry and Physics, 22(12), 8037-8057.

Zhang, P., Chen, G., Ting, M., Ruby Leung, L., Guan, B., & Li, L. (2023). More frequent atmospheric rivers slow the seasonal recovery of Arctic sea ice. *Nature Climate Change*, *13*(3), 266-273.